# PCCP

Physical Chemistry Chemical Physics

## Accepted Manuscript

## PCCP

Physical Chemistry Chemical Physics
rsc.li/pccp

ISSN 1463-9076

PAPER
H.-P. Loock et al.
Determination of the thermal, oxidative and photochemical degradation rates of scintillator liquid by fluorescence EEM spectroscopy

ROYAL SOCIETY OF CHEMISTRY

rsc.li/pccp

# ARTICLE

## Unveiling thermolysis natures of ZIF-8 and ZIF-67 employing *in situ* structural characterizations

Chunhui Wu,[b] Donggang Xie,[b] Yingjie Mei,[a] Zhifeng Xiu,[b] Kristin M. Poduska,[c] Dacheng Li,[d] Ben Xu,[a, b*] and Daofeng Sun [a, b]

Thermolysis routes of two isostructural metal-organic framework compounds (Zn-based ZIF-8 and Co-based ZIF-67) are investigated based on temperature-dependent and time-dependent *in situ* Fourier transform infrared (FTIR) spectroscopy and *in situ* X-ray diffraction data, as well as thermogravimetric-differential scanning calorimetry (TG-DSC) analyses and density functional theory (DFT) calculations. These data highlight thermolysis effects on different vibrations and dissociations within specific atomic moieties. The coordination differences between Zn-N and Co-N lead to the distinct thermolysis routes of ZIF-8 and ZIF-67. ZIF-8 is easy-deformed during heating while can maintain at a higher temperature due to the satruated Zn-N coordination. ZIF-67, however, does not deform during heating due to the stronger Co-N bonds, while easy-reactive to oxygen due to the unsaturated Co-N bonds. Our results demonstrate that *in situ* FTIR pared with *in situ* XRD is powerful techniques for MOF thermolysis investigation, and we suggest that the thermolysis mechanisms of MOFs may be unveiled by investigating in a series of MOFs having different coordination types using the *in situ* characteristic methods.

## Introduction

Metal-organic frameworks (MOFs) are novel porous materials having periodic structures constructed of metal centres and bridging ligands.[1, 2] Due to their regular and adjustable pore sizes, as well as the unsaturated sites of the metal centres, they are ideal for applications involving gas separation/storage, water treatment, catalysis, and sensing.[3-8] MOFs are also commonly used as precursors to prepare carbon- or metal-based or composite nanomaterials for energy and environmental applications.[9-12] One commonly used method of transforming MOFs into composite nanomaterials is thermolysis, and many promising results have been reported.[13-16] Furthermore, the novel MOF glasses are also commonly produced through heating Zn or Co based ZIFs.[17, 18] However, thermolysis of a MOF is a complicated process, during which many chemical and physical variations occur. MOFs can differ in their metal centers, organic ligands, and topological features. These differences influence MOF thermolysis, but have not yet been deeply investigated. Thus, it is challenging to select proper thermolysis conditions to regulate the thermolysis routes of MOFs.

ZIF-8 and ZIF-67 are widely reported MOF precursors for nanomaterial preparation. They are isostructural with the same organic ligands of 2-methylimidazole and similar lattice constants, but they have different metal centers: ZIF-8 is Zn-based, while ZIF-67 is Co-based.[19-23] This single difference causes dramatically different thermal stabilities: ZIF-67 decomposes ~300 ℃ in air, while ZIF-8 decomposes almost 100 ℃ higher.[24] This enable us to reveal the influences of metal centers on the thermolysis behaviors of ZIF-8 and ZIF-67. Furthermore, understanding the thermolysis routes of ZIF-8 and ZIF-67 can guide the applications of ZIF-8 and ZIF-67, especially under high temperature conditions.

To probe structural variations rapidly throughout the MOF thermolysis process, in situ measurements during heating are ideal.[25-27] Furthermore, it is imperative that the measurements themselves do not add extra energy to the system to induce spurious structural and/or compositional changes to the samples. For this reason, it is helpful to combine multiple experimental and theoretical tools to ensure the data is interpreted consistently. X-ray diffraction (XRD) methods are well established in MOF studies to provide essential details about crystal structure transformations through changes in peak positions and intensities. Fourier transformed infrared (FTIR) spectroscopy yields vibration-based peak positions, intensities, and shapes that contain abundant information about crystal structure, bonding environments, and chemical compositions. Not only is the collection of one FTIR spectrum fast, the infrared photons are relatively low in energy and

a. *College of Material Science and Engineering, China University of Petroleum (East China), Qingdao, Shandong, 266580, PR China.*

b. *College of Science, China University of Petroleum (East China), Qingdao, Shandong, 266580, PR China.*

c. *Department of Physics and Physical Oceanography, Memorial University of Newfoundland, St. John's, NL, A1B3X7, Canada.*

d. *Shandong Provincial Key Laboratory of Chemical Energy Storage and Novel Cell Technology, School of Chemistry and Chemical Engineering, Liaocheng University, Liaocheng, Shandong, 252059, PR China*

Corresponding author: Ben Xu benxu@upc.edu.cn

**ARTICLE**

**Journal Name**

generally do not induce sample damage.[28, 29] FTIR spectra of MOFs can be simulated via density functional theory (DFT) calculations, which allows each experimentally observed FTIR peak to be assigned to a specific vibrational mode. By correlating XRD, FTIR, and DFT data, it is possible to follow temperature induced structural changes in detail.

In this work, we give the first report that compares the different thermolysis routes of ZIF-8 and ZIF-67 using in situ (during heating) FTIR. These data are combined with thermogravimetric analysis – differential scanning calorimetry (TGA-DSC), in situ (during heating) XRD, and DFT calculations to assign FTIR peaks and to investigate the structural variations of ZIF-8 and ZIF-67 during heating, for unveiling their thermolysis mechanisms through understanding the influences of their different metal centres.

## Experimental details

### Synthesis of ZIF-8 and ZIF-67

The synthesis of ZIF-8 and ZIF-67 were based on previous reports.[30] A 25 mL methanol-based solution of $Zn(NO_3)_2 \cdot 6H_2O$ (0.3028 g, 1.018 mmol) or $Co(NO_3)_2 \cdot 6H_2O$ (0.2942 g, 1.010 mM) was rapidly poured into 25 ml of a methanol-based solution of 2-methylimidazole (0.3287 g, 4.004 mM) at ambient temperature. The mixture was stirred with a magnetic bar for 10 minutes until the ZIF started crystallizing. The mixture then sat undisturbed for the subsequent 24 hours. The resulting precipitants were centrifuged and rinsed with methanol three times, then dried at 60℃ overnight before storage at ambient temperature.

### Characterization methods

TGA-DSC data (Mettler Toledo TGA/DSC1) were collected from room temperature (25℃) to 900℃ with a heating rate of 2 ℃ per minute while under compressed air flow. XRD data (Rigaku Ultima IV system with Cu K⍺ radiation) were collected over a range of 3-45 degrees (2theta). For the *in situ* XRD studies, the temperature ranged from 30-450 ℃ for ZIF-8 and 30-350 ℃ for ZIF-67. Transmittance FTIR spectra (PerkinElmer Frontier) were collected in the range of 4000-400 cm⁻¹ with 1 cm⁻¹ resolution and 4 scans. These parameters enable one spectrum to be collected in 40 seconds.

FTIR transmittance spectra were collected using samples that were "drop-coated" on IR-transparent KBr windows.  It is more common to finely grind the sample, combine it with a large amount of IR-transparent powder (such as NaCl or KBr, at a 1:50 ratio), and then press it into a pellet.[21] However, in this case, most of the sample of interest will be encased within the pellet and have limited access to the open air. Since the availability of $O_2$ influences the MOF thermolysis routes and products, we chose to avoid pellets. In our drop-coating procedure, a small amount of sample was sonicated in ethanol for 10 minutes, then allowed to sit for 1 hour to allow the largest particles to sediment. Subsequently, one or two drops of the supernatant containing smaller sample grains were dripped on a 13 mm diameter KBr window and allowed to dry in air. The reason that only the samples with smaller particle sizes were selected is that

larger particle sizes (larger than the wavelength of the incident IR light) will cause asymmetric peaks due to the "Christiansen effect".[30]

For all *temperature-dependent* XRD and FTIR measurements, the samples were heated from room temperature to either 425 ℃ (ZIF-8) or 400 ℃ (ZIF-67) at intervals of 25 ℃, with a hold at each temperature step for 15 minutes before collecting the spectrum. Data were collected every 10 minutes, and the total heating time was 2 hours. For *time-dependent measurements* at high temperatures, samples were held at a temperature just above their thermal decomposition threshold (375 ℃ for ZIF-8 and 300 ℃ for ZIF-67) for two hours.

The temperature control for the XRD studies was based on a Rigaku-D8 XRD equipment. However, for the FTIR heating studies, the set-up was custom-designed, as described in detail elsewhere.[21] A ceramic heater and a K-type thermocouple (0-900℃) were both wired to a proportional-integral-derivative (PID) temperature monitor and controller (working range -199 to 1000 ℃).  To hold the sample, a heating stage wrapped with thermal insulation was sealed in a frame, both of which were made of thermal-insulated ceramic fibers. A commercial infrared thermometer was used to validate the accuracy of the temperature readings at the sample stage prior to the start of the experiments. A 10 mm diameter aperture in the heating stage allowed the IR beam to reach the sample.

### Computational details

Electronic structure calculations were carried out using DFT in a plane wave pesudopotential implementation using the CASTEP code in Material Studio.[31-33] Due to the fact that ZIF-8 and ZIF-67 are isostructural, their FTIR spectra are nearly identical. Therefore, we calculated the FTIR spectrum of ZIF-8 alone. However, we did calculate metal-ligand bond energies for both ZIF-8 and ZIF-67.

The ZIF-8 and ZIF-67 crystals were built based on the reported lattice parameters.[30] We used a conventional cell (276 atoms total) and then relaxed the atomic positions. The GGA+PBESOL exchange-correlation function was then employed, and self-consistent field tolerance of $1.0 \times 10^{-6}$ eV/atom was set for the convergence. An FFT grid of 135*135 *135 and the Monkhorst-Pack k-point of 1*1*1 were adequate for these studies.  Norm conserving pseudopotentials were used to represent ionic cores, and the pseudopotential files used for hydrogen, carbon, nitrogen, and zinc were H_00PBE_OP.recpot, C_00PBE_OP.recpot, N_00PBE_OP.recpot, and Zn_00.recpot.

## Results and discussions

Off situ FTIR measurement were utilized to confirm the isostructural relation of ZIF-8 and ZIF-67 based on their very similar in terms of peak positions and intensities (Figure S1). In order to better understanding the vibration associated IR peaks, the FTIR spectra were collected using "coated KBr windows" instead of KBr pellets, and the details are described in the supplementary information. Furthermore, DFT calculations were performed to assign the proper vibrations to the IR peaks, as shown in Figure S1 and Table S1. Representative SEM images (Fig. S1 c and d) indicate that both ZIF-8 and ZIF-67 exhibits polyhedron-shaped crystallites with the size of around 100 nm.

**Journal Name**

**ARTICLE**

Consistent with others,[24] TGA-DSC results in Figure 1a and 1b reveal their distinct thermolysis routes. ZIF-8 slowly decreases its TG value up to 300 ℃, followed by a more drastic decline. This drop has two distinct steps (300-450 ℃, and 450-550 ℃) that are associated with DSC peaks near 400 ℃ and 550 ℃, indicating that the thermolysis of ZIF-8 undergoes two separate heat-release processes. In contrast, ZIF-67 has a much more rapid weight loss near 300 ℃, and the associated overlapping DSC peaks imply that three different heat-release reactions occur almost simultaneously.

The *in situ* temperature-dependent FTIR spectra of ZIF-8 (25-425 ℃) and ZIF-67 (25-375 ℃) are exhibited in Figure 1c. The sudden drops at 400 ℃ for ZIF-8 and at 325 ℃ for ZIF-67 are associated with sample loss due to thermolysis. In the lower wavenumber region, broad rise between 600 and 400 $cm^{-1}$ in the ZIF-8 spectra indicates the formation of ZnO, and the growing double peaks centered at 650 and 555 $cm^{-1}$ in the ZIF-67 spectra are due to $Co_3O_4$. The intensities of most ZIF-8 peaks start to drop above 350 ℃, while ZIF-67 peaks suddenly drops at 325 ℃. These transition temperatures are consistent with the TGA-DSC data.

Although the *in situ* FTIR spectra of ZIF-67 and ZIF-8 present the similar variations, a noticeable difference appears in the peak related to C=C stretching (1580 $cm^{-1}$, as highlighted in Figure 1c). A shoulder at the higher wavenumber side of this peak arises for ZIF-8 above 325 ℃. In contrast, the 1570 $cm^{-1}$ peak in the spectra of ZIF-67 exhibits homogeneous broadening, and no shoulder appears. Based on these data, we suspected that ZIF-8 undergoes deformation before decomposition, while ZIF-67 does not.
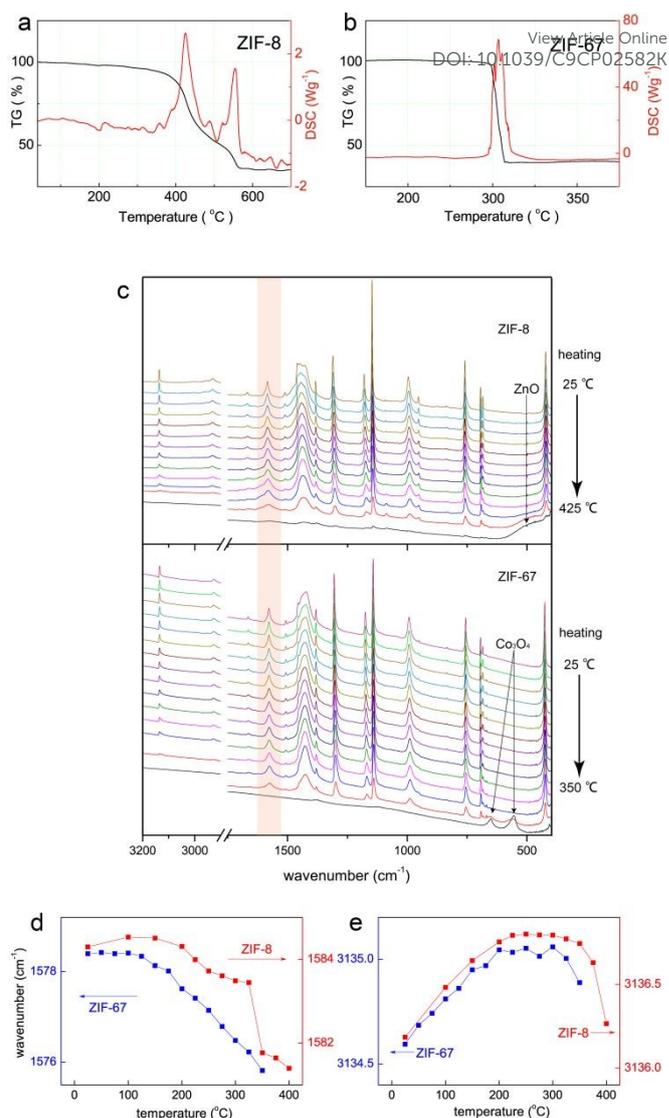


Figure 1 The TGA-DSC results of ZIF-8 (a) and ZIF-67 (b). Temperature dependent *in situ* FTIR spectra of ZIF-8 and ZIF-67 (c). IR peak shifting of C=C stretching (d) and $H_{ring}$ symmetric stretching (e).

More detailed analysis in the peak positions, peak intensities, and peak widths are therefore performed to investigate this difference, and the results are presented in Figure 1d, 1e, and Figure S2 to S7. FTIR peak positions depend on the energies of vibration modes within the solid, which can be significantly affected by changes in atomic arrangements,[25, 31] and the peak position variations clearly demonstrate how lattice changes during heating. Most peaks (for both ZIF-8 and ZIF-67) exhibit smooth red-shifting that can be attributed to lattice expansion during heating. The $H_{ring}$ symmetric stretch peaks (3137 $cm^{-1}$ for ZIF-8 and 3135 $cm^{-1}$ for ZIF-67) exhibit initial blue-shifting followed by red-shifting, which is associated with the expanded aromatic rings in ZIFs leading to decreased $H_{ring}\cdots H_{ring}$ distances, hardening the $H_{ring}$ symmetric stretch in both ZIF-8 and ZIF-67.[27] The similar peak position changes, as well as the similar changes in peak intensities and widths, indicate that most fractions of ZIF-8 and ZIF-67 lattices experience similar variations during heating.

However, the temperature-dependence of the C=C stretch (Figure 1d) shows a qualitative difference between ZIF-8 and ZIF-67. For ZIF-

8, there is discontinuity in the peak position shift near 325 ℃, which is slightly lower than the onset of the decomposition that we see in its TGA-DSC data (Figure 1b). Considering this temperature is also where the shoulder on this FTIR peak appears, we believe that ring deformation causes the shoulder, occurring before the lattice collapse. In contrast, the C=C stretch for ZIF-67 has a smooth peak shift between 175 ℃ to 350 ℃, suggesting a direct collapse of its lattice structure without lattice deformation.

To help decouple structural changes within atomic moieties from overall lattice expansion effects, we used temperature-dependent i*n situ* XRD measurements (Figure 2). It is evident that XRD peak intensities for ZIF-8 drop significantly at 450 ℃, while those of ZIF-67 disappear at 350 ℃; this is consistent with transition temperatures we identified in TGA-DSC data (Figure 1a and 1b) and the *in situ* FTIR results (Figure 1c). There is an interesting difference in the XRD peak shifts as a function of temperature between the two ZIF compounds. While all ZIF-67 peaks shift to smaller 2theta angles (signifying an overall lattice increase), only the ZIF-8 peaks at larger 2-theta angles (greater than 13) shift to lower values. The remaining peaks at smaller 2-theta values shift to higher angles.

To make sense of these different XRD peak shifts, it helps to consider the different *hkl* planes associated with the anomalous (upward-shifting) peaks. The insets at the top of Figure 2a and 2b highlight four selected peaks to illustrate the differences in the peak shifting trends. For ZIF-67, all four selected XRD peaks shift to lower 2-theta values, implying a regular lattice expansion due to heat. For ZIF-8, the (011) peak at 7.2 corresponds to an inter-planar distance related to the width of the ZIF frame (Figure 2c and S8). This peak shows negligible shift below 350 ℃, above which it shifts to slightly higher angles, implying a shrinking frame. Above 450 ℃, the peak shifts to smaller 2-theta again, indicating that the enlarged frame. Furthermore, the (011) peak intensity weakens, implying destruction of the frames. The (211) peak position shows a temperature-dependent trend that is similar to the (011) peak. However, the (222) and (413) peaks, which correspond to smaller inter-planar distances within the ZIF-8 subunit, shift consistently to lower wavenumbers as temperature increases.
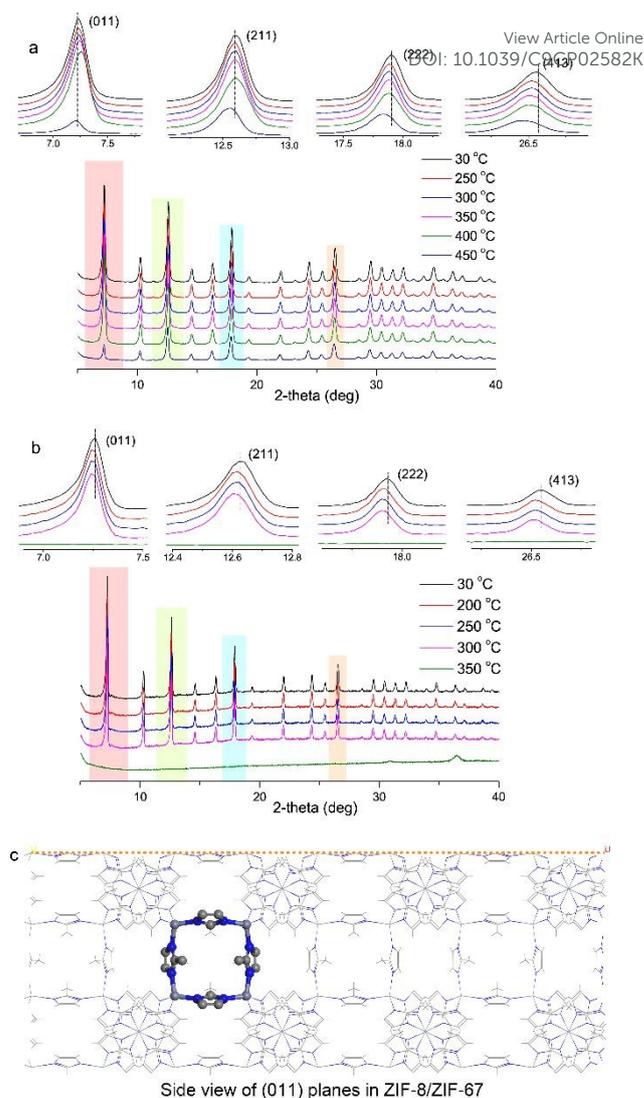


Figure 2 Temperature-dependent (in situ) XRD data for (a) ZIF-8 and (b) ZIF-67. Enlarged views of selected (highlighted) peaks are displayed above the full spectra. (c) is a schematic representation of the (011) planes (dotted orange line) that shows their relation to the MOF frame.

Considering in more detail the peak intensity variations as a function of temperature, all ZIF-8 peaks persist in the XRD patterns, without new peaks appearing, indicating that the structure of ZIF-8 is maintained. As discussed above, the (011) peak shows a much more significant intensity decrease than the other peaks. Therefore, we can conclude that the thermolysis distorts the ZIF-8 frame by altering the Zn-N bonds, leaving the 2-mety-imidazole rings largely preserved. For ZIF-67, its thermolysis occurs so rapidly above 300 ℃ (see TGA data in Figure 1b) that XRD data related to its intermediate structural changes were not obtainable.

Based on our results, we understand the thermolysis routes of these two isostructural MOFs in the following way, as presented in Figure 3. Both compounds exhibit heating-induced expansion, leading to shifts of most IR peaks to lower wavenumbers and shifts of most XRD peaks to smaller 2-theta angles. However, ZIF-8 behaves differently in that it undergoes a complicated deformation from 325

**Journal Name**

**ARTICLE**

to 400 ℃ as its frame shrinks, indicated by the shift of the (011) XRD peak to larger 2-theta angles. Meanwhile, the deformed lattice of ZIF-8 drastically influence the "C=C windows" (Figure S9), and the C=C stretching IR peak present abnormality. Other fractions, including the imidazole rings and methyls, only present regular expansion during heating.
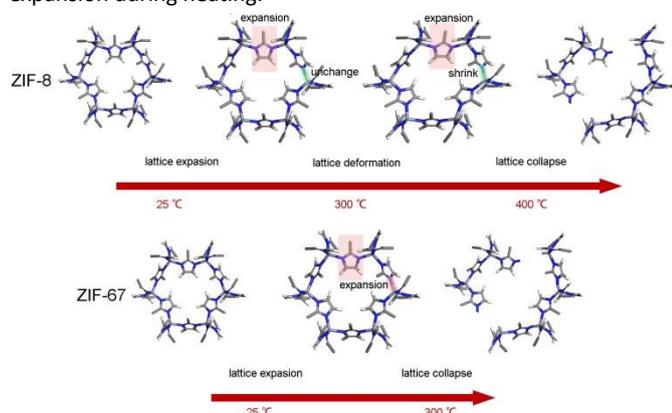


Figure 3 A schematic comparison of thermolysis routes for ZIF-8 and ZIF-67 in air. ZIF-8 experiences deformation around 300 ℃, and it slowly collapses from 350 to 550 ℃. ZIF-67 rapidly collapses at 300 ℃.

The frames of either ZIF-8 or ZIF-67 are composed of the Zn/Co-N bonds and the imidazole rings. It has been reported that the Zn-N bonds are more easily broken under heating than the imidazole rings,[32] and thus, it is reasonable to correlate the different thermolysis routes of ZIF-8 and ZIF-67 to their different metal-nitrogen bonds. DFT calculations were therefore conducted to investigate the bonding energies of Zn-N and Co-N, and the Zn-N bond energy of 2.075 eV is actually much lower than Co-N bond energy of 2.834 eV. We believe the higher Co-N bond energy is due to the higher electronegativity (EN) of Co (EN=1.88) compared with Zn (EN=1.65).[18] The higher bond energy within Co-N indicates ZIF-67 lattice is less deformed during heating compared with ZIF-8. Actually, other researchers also have reported that the ZIF-8 lattice is soft, and those gas molecules with kinetic diameters larger than its window can still pass throug,[22, 33] further support our conclusions.

However, the stronger Co-N bonds cannot explain the much lower thermolysis temperature of ZIF-67. Here, we suggest the coordination type is the domain reason. A cobalt atom has an outer shell of $3d^7 4s^2$, leading to the unsaturated coordinating to nitrogen atoms in ZIF-67. A zinc atom presents the $3d^{10} 4s^2$ outer shell, and the Zn-N coordination is saturated. Therefore, although Co-N has a higher bonding energy than Zn-N, it is still more prone to oxygen during heating since its unsaturation.
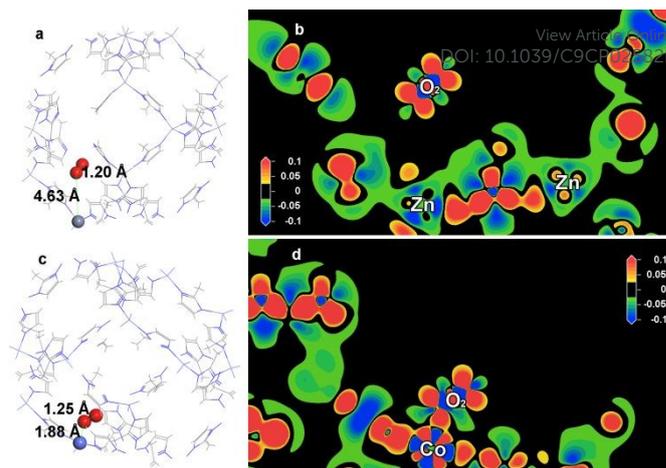


Figure 4 The optimized ZIF-8 (a) and ZIF-67 (c) frames with one molecule placed inside the frames. The Co-O distance of 1.88 Å is evidently much shorter than the Zn-O distance of 4.63 Å. The charge density differences plots of ZIF-8 (b) and ZIF-67 (d) further demonstrate that the Co site is prone to the attack from $O_2$.

DFT calculations were further employed to illustrate the easier coordination of $O_2$ to the Co site compared with ZIF-8. As demonstrated in Figure 3, Video S1 (ZIF-8) and Video S2 (ZIF-67), one $O_2$ molecule was placed close to the metal sites inside the frames, and the frames were relaxed. It is clear that the $O_2$ molecule moves away from Zn in ZIF-8 while stays with Co in ZIF-67. Furthermore, the ZIF-67 frame experiences an evidently deformation, implying its easy-deformed lattice under the $O_2$ atmosphere during heating. The charge density differences plots further demonstrate that the Co site is prone to the attack from $O_2$. It is clear that the Co is in the unsaturated D2-SP3 hybridization and that Zn is in the saturated SP3 hybridization. $O_2$ is bonded to Co due to its unsaturation within ZIF-67. For ZIF-8, however, the saturated Zn sites within it do not perform coordination to the $O_2$ molecule.

The similar investigations of the decomposition temperatures of ZIF-62(Co) and ZIF-62(Zn) are associated with our conclusions.[18] Co-N in ZIF-62(Co) is stronger than ZIF-62(Zn). However, the decomposition temperature of ZIF-62(Co) in $N_2$ is lower compared with ZIF-62(Zn), and we suggest that the reason is also attributed to the unsaturated Co-N bonds.

The unsaturated Co-N bond also leads to the rapid themolysis (reaction) rate of ZIF-67 in air, supported by the TGA results. However, the thermolysis or reaction rate of the ZIF materials cannot be quantitatively investigated. Therefore, we monitored FTIR peak intensity changes which are associated with the sample lost. Incident IR light ($I_0$) is absorbed based on the absorption coefficient for the specified vibrational mode ($\mu$), and the quantity of sample in the light's path ($t$), yielding transmitted light $(I)$, according to this expression:[34]

$$I = I_0\, exp^{-\mu t}$$

In our case, the intensities were measured per unit of absorbance ($\mu t$). Since $\mu$ is a constant for a given vibrational mode, we attribute decreases in peak intensity to be proportional to a decrease in the amount of MOF as it decomposes. Based on this, we evaluate the

**ARTICLE**

thermolysis rate by analysing the time-dependence of FTIR peak intensity decreases.
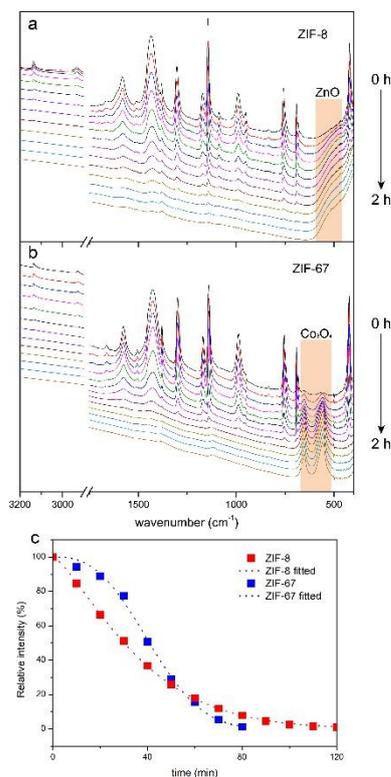


Figure 5 Time-dependent high-temperature (*in situ)* FTIR spectra of ZIF-8 (a) and ZIF-67 (b), over a span of 2 hours, at 375 ℃ and 300 ℃ , respectively. The vertical axes are scaled and offset for clarity, and the peaks corresponding to the decomposition products (either ZnO or Co₃O₄) are highlighted. (c) A representative plot of FTIR peak intensity drop with increasing time, shown here for the H$_{ring}$ wag (1140 cm$^{-1}$).

Time-dependent *in situ* FTIR spectra of ZIF-8 (at 375 ℃) and ZIF-67 (at 300 ℃) are presented in Figure 3. Based on the temperature-dependent *in situ* FTIR results, the IR peaks start dropping at 375 ℃ for ZIF-8 and at 300 ℃ for ZIF-67, and thus, these temperatures were selected. The detailed analyses of the changes in peak intensities, as well as positions and widths, as functions of time are shown in Figures S10-S15. The simultaneous drops in peak intensities with increasing time indicates gradual loss of ZIFs. All peaks present the similar variation trend, indicating that the decomposition occur within the whole frame, rather than specific fractions. One representative example, the H$_{ring}$ wag (1140 cm$^{-1}$), the strongest peak in either ZIF-8 or ZIF-67 spectrum, is presented in Figure 5c. To compare the relative thermolysis (reaction) rates, we fit the H$_{ring}$ wag intensity *vs.* time data to the modified isothermal Avrami model:[35]

$$\alpha = exp[-(kt)^n]$$

where *k* is the thermolysis (reaction) rate constant, *n* is the Avrami exponent (1<n<4), *t* is time, and $\alpha$ is the residual amount of ZIFs. Avarami's model can be used to describe the transformation kinetics of many solid state processes under isothermal conditions, and the kinetic exponent, *n*, has characteristic values based on some simple

cases. Previous reports indicate that, for diffusion controlled growth, an *n* value larger than 2.5 indicates an increasing rate, while an *n* value of 1.5 corresponds to a constant rate.[35] Our fits (Figure 3c and Table S2) suggest that ZIF-8 data has an *n* value of 1.33±0.01, consistent with a constant reaction rate, while ZIF-67 has n = 2.7±0.1, consistent with an increasing reaction rate. Thus, it is reasonable concluded that the oxidation of Co in ZIF-67 further accelerates the reaction, which is likely associated with the heat-release feature from the DSC result (Figure 1b). The thermolysis of ZIF-8, however, occurs in a smooth and gradual way in constant rate.

It is worth mentioning that all IR peak drops at the constant positions, and therefore, it is less possible that some fractions preferentially dissociate from either ZIF-8 or ZIF-67. Furthermore, from the IR spectra, we did not notice any intermediates, and we suggest that the CO$_x$ and NO$_x$ volatiles are produced during the collapse. However, previous studies of Lin et. al. suggest that there are intermediates during decomposition of ZIF-8.[36] One possible reason is that they heated ZIF-8 at 300 ℃ for 20 hours, and the decomposition rate is much slower compared with the heating temperature of 350 ℃, which is the condition employed during our measurements. And therefore, the intermediates they reported likely rapidly decomposed at 350 ℃, and we were not able to find them. Off situ NMR experiments were also conducted to further demonstrate that there is no organic by-product during heating for either ZIF-8 and ZIF-67, as shown in Figure S16.

## Conclusions

Thermolysis of MOFs is a widely reported strategy for functional nanomaterial preparation, yet thermolysis pathways are poorly understood and not necessarily generalizable. It is well known that MOF functionalities can be tuned with different metal centers, organic ligands, and topological features. This means that it is challenging to select a proper temperature and atmosphere for thermolyzing MOF precursors in order to decompose them into the desired nanomaterial products. Thus, in order to achieve a more effective and precise control of the thermolysis processes of MOF precursors, it is essential to understand the influences of the structural and compositional variations of MOFs during heating, as we do in this study.

Our work on ZIF-8 and ZIF-67 serves two purposes. First, it illustrates that *in situ* FTIR along with *in situ* XRD pair well to understand the structural and compositional variations that occur at different stages MOF thermolysis. Second, it demonstrates that the coordination between metal centers and organic ligands are the dominant factor influencing the thermolysis behaviors. Due to the stronger coordination of Co-N compared with Zn-N, ZIF-67 hardly deforms during heating, while the ZIF-8 frame deforms before thermolyzing, and the deformation mainly occurs to the "window", i.e. the Zn-N bonds. Although Co-N bonds are stronger, the unsaturated coordination of Co-N causes the more reactivity of Co to oxygen, and leading to a much faster thermolysis kinetic at much lower thermolysis temperature in air compared with ZIF-8.

Looking forward, we suggest that it could be possible to predict the thermolysis behaviors by investigating a series MOFs using *in situ* FTIR and XRD measurements. By investigating systematic trends in

the thermolysis behaviors, we suggest that the thermolysis routes could be regulated by utilizing proper atmospheres, temperatures, and heating rates. This would be especially useful for MOFs with mixed ligands and mixed metal centers that have been widely reported, providing the possibility of "selecting-fraction-thermolysis" and novel porous structures.[37]

## Conflicts of interest

There are no conflicts to declare.

## Acknowledgements

## References

1.  S. L. James, *Chem. Soc. Rev.*, 2003, **32**, 276.
2.  E. Adatoz and S. Keskin, *Journal of Nanomaterials*, 2015, **2015**, 1-9.
3.  T. Zhang and W. Lin, *Chem. Soc. Rev.*, 2014, **43**, 5982-5993.
4.  N. Kornienko, Y. Zhao, C. S. Kley, C. Zhu, D. Kim, S. Lin, C. J. Chang, O. M. Yaghi and P. Yang, *J. Am. Chem. Soc.*, 2015, **137**, 14129-14135.
5.  Z. Hasan and S. H. Jhung, *J. Hazard. Mater.*, 2015, **283**, 329-339.
6.  E. M. Dias and C. Petit, *J. Mater. Chem. A*, 2015, **3**, 22484-22506.
7.  D. Sheberla, J. C. Bachman, J. S. Elias, C. J. Sun, Y. Shao-Horn and M. Dinca, *Nat Mater*, 2017, **16**, 220-224.
8.  J. A. Villajos, G. Orcajo, C. Martos, J. Á. Botas, J. Villacañas and G. Calleja, *Int. J. Hydrogen Energy*, 2015, **40**, 5346-5352.
9.  R. Fang, R. Luque and Y. Li, *Green Chemistry*, 2016, **18**, 3152-3157.
10.  J. Liu, D. Zhu, C. Guo, A. Vasileff and S.-Z. Qiao, *Adv. Energy Mater.*, 2017, **7**, 1700518.
11.  T. Deng, Y. Lu, W. Zhang, M. Sui, X. Shi, D. Wang and W. Zheng, *Adv. Energy Mater.*, 2018, **8**, 1702294.
12.  S. J. Yang, T. Kim, J. H. Im, Y. S. Kim, K. Lee, H. Jung and C. R. Park, *Chem. Mater.*, 2012, **24**, 464-470.
13.  F. Zou, Y. M. Chen, K. Liu, Z. Yu, W. Liang, S. M. Bhaway, M. Gao and Y. Zhu, *ACS Nano*, 2016, **10**, 377-386.
14.  R. Bendi, V. Kumar, V. Bhavanasi, K. Parida and P. S. Lee, *Adv. Energy Mater.*, 2016, **6**, 1501833.
15.  X. Xu, R. Cao, S. Jeong and J. Cho, *Nano Lett.*, 2012, **12**, 4988-4991.
16.  R. R. Salunkhe, J. Tang, Y. Kamachi, T. Nakato, J. H. Kim and Y. Yamauchi, *ACS Nano*, 2015, **9**, 6288-6296.
17.  A. W. Thornton, K. E. Jelfs, K. Konstas, C. M. Doherty, A. J. Hill, A. K. Cheetham and T. D. Bennett, *Chem. Commun. (Camb.)*, 2016, **52**, 3750-3753.
18.  L. Frentzel-Beyme, M. Kloß, R. Pallach, S. Salamon, H. Moldenhauer, J. Landers, H. Wende, J. Debus and S. Henke, *J. Mater. Chem. A*, 2019, **7**, 985-990.
19.  X. Wang, J. Liu, S. Leong, X. Lin, J. Wei, B. Kong, Y. Xu, Z. X. Low, J. Yao and H. Wang, *ACS Appl. Mater. Interfaces*, 2016, **8**, 9080-9087.
20.  C. H. Kuo, Y. Tang, L. Y. Chou, B. T. Sneed, C. N. Brodsky, Z. Zhao and C. K. Tsung, *J. Am. Chem. Soc.*, 2012, **134**, 14345-14348.
21.  D. Yu, B. Wu, L. Ge, L. Wu, H. Wang and T. Xu, *J. Mater. Chem. A*, 2016, **4**, 10878-10884.
22.  P. Krokidas, M. Castier, S. Moncho, D. N. Sredojevic, E. N. Brothers, H. T. Kwon, H.-K. Jeong, J. S. Lee and I. G. Economou, *J. Phys. Chem. C*, 2016, **120**, 8116-8124.
23.  J. Tang, R. R. Salunkhe, J. Liu, N. L. Torad, M. Imura, S. Furukawa and Y. Yamauchi, *J. Am. Chem. Soc.*, 2015, **137**, 1572-1580.
24.  A. F. Gross, E. Sherman and J. J. Vajo, *Dalton Trans*, 2012, **41**, 5458-5460.
25.  B. Xu, Y. Mei, Z. Xiao, Z. Kang, R. Wang and D. Sun, *Phys. Chem. Chem. Phys.*, 2017, **19**, 27178-27183.
26.  S. M. Kim, W.-C. Liao, A. M. Kierzkowska, T. Margossian, D. Hosseini, S. Yoon, M. Broda, C. Copéret and C. R. Müller, *Chem. Mater.*, 2018, **30**, 1344-1352.
27.  G. Kumari, K. Jayaramulu, T. K. Maji and C. Narayana, *J. Phys. Chem. A*, 2013, **117**, 11006-11012.
28.  Y. Hu, H. Kazemian, S. Rohani, Y. Huang and Y. Song, *Chem. Commun.*, 2011, **47**, 12694-12696.
29.  A. Greenaway, B. Gonzalez-Santiago, P. M. Donaldson, M. D. Frogley, G. Cinque, J. Sotelo, S. Moggach, E. Shiko, S. Brandani, R. F. Howe and P. A. Wright, *Angew. Chem. Int. Ed.*, 2014, **53**, 13483-13487.
30.  D. Saliba, M. Ammar, M. Rammal, M. Al-Ghoul and M. Hmadeh, *J. Am. Chem. Soc.*, 2018, **140**, 1812-1823.
31.  B. Xu and K. M. Poduska, *Phys. Chem. Chem. Phys.*, 2014, **16**, 17634-17639.
32.  S. Gadipelli, W. Travis, W. Zhou and Z. Guo, *Energy Environ. Sci.*, 2014, **7**, 2232-2238.
33.  H. T. Kwon, H. K. Jeong, A. S. Lee, H. S. An and J. S. Lee, *J. Am. Chem. Soc.*, 2015, **137**, 12304-12311.
34.  K. M. Poduska, L. Regev, E. Boaretto, L. Addadi, S. Weiner, L. Kronik and S. Curtarolo, *Adv. Mater.*, 2011, **23**, 550-554.
35.  J. Málek, *Thermochim. Acta*, 1995, **267**, 61-73.
36.  J. B. James and Y. S. Lin, *J. Phys. Chem. C*, 2016, **120**, 14015-14026.
37.  L. Feng, S. Yuan, L. L. Zhang, K. Tan, J. L. Li, A. Kirchon, L. M. Liu, P. Zhang, Y. Han, Y. J. Chabal and H. C. Zhou, *J. Am. Chem. Soc.*, 2018, **140**, 2363-2372.

# Supporting Information

# Unveiling thermolysis pathways of ZIF-8 and ZIF-67 by employing *in situ* structural characterizations

Chunhui Wu,[b] Donggang Xie,[b] Yingjie Mei,[a] Zhifeng Xiu,[b] Kristin M. Poduska,[c] Dacheng Li,[d] Ben Xu,[a, b*] and Daofeng Sun [a, b]


a. College of Material Science and Engineering, China University of Petroleum (East China), Qingdao, Shandong, 266580, People's Republic of China.

b. College of Science, China University of Petroleum (East China), Qingdao, Shandong, 266580, People's Republic of China.

c. Department of Physics and Physical Oceanography, Memorial University of Newfoundland, St. John's, NL, A1B3X7, Canada.

d. Shandong Provincial Key Laboratory of Chemical Energy Storage and Novel Cell Technology, School of Chemistry and Chemical Engineering, Liaocheng University, Liaocheng, 252059, People's Republic of China
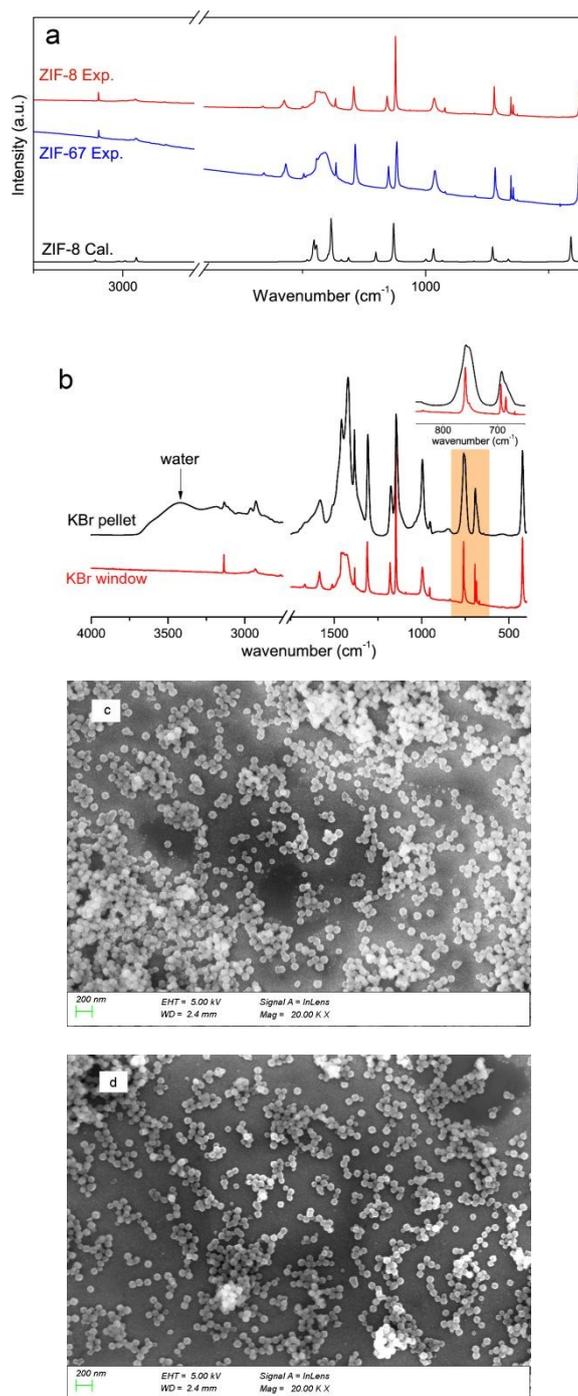
Fig. S1 The *ex situ* FTIR spectra of ZIF-8 and ZIF-67 (a), and comparison between the FTIR spectra of ZIF-8 collected using KBr pellets and KBr windows. The inset shows the zoomed-in peaks from 850 to 650 cm$^{-1}$. The spectrum collected using the KBr window (b) displays much sharper and narrower peaks. The narrower peaks are due to the smaller and more uniform ZIF-8 particle sizes during the KBr window measurement. Representative SEM images of "drop-coated" ZIF-8 and ZIF-67 samples are shown in (c) and (d).

Table S1. Peak positions and vibrational mode assignments for ZIF-8 (experiment and calculated) and ZIF-67 (experiment).

| Band assignment[a] | ZIF-8 Exp. (cm$^{-1}$) | ZIF-67 Exp. (cm$^{-1}$) | ZIF-8 Cal. (cm$^{-1}$)[b] |
|---|---|---|---|
| Methyl in-plane bend (S) | 422 | 425 | 410 (-12) |
| Ring out-of-plane bend (M) | 685 | 685 | 665 (-20) |
| Methyl stretch (S) | 694 | 694 | 683 (-11) |
| H$_{ring}$ symmetric out-of-plane bend (S) | 759 | 756 | 728 (-31) |
| H$_{ring}$ asymmetric out-of-plane bend (VW) | 837 | 8359 | 804 (-33) |
| Ring in-plane bend (W/VW) | 953 | 952 | 932 (-21) |
| H$_{methyl}$ bend (S) | 995 | 992 | 971 (-24) |
| H$_{ring}$ scissor + H$_{methyl}$ bend (VW) | 1091 | - | 998 (-93) |
| H$_{ring}$ wag (VS/S) | 1147 | 1142 | 1130 (-17) |
| Ring breathing (C-N symmetric stretch) (S) | 1180 | 1175 | 1201 (21) |
| H$_{methyl}$ scissor(M) | 1311 | 1304 | 1312 (1) |
| Ring deformation (C-N asymmetric stretch) (S) | 1380 | 1381 | 1342 (-38) |
| H$_{methyl}$ bend (S) | 1400~1500 | 1400~1500 | 1380~1420 |
| C=C stretch+C$_{ring}$-C$_{methyl}$ stretch (W) | 1512 | 1507 | 1442 (-70) |
| Ring breathing (C=C stretch) (M) | 1584 | 1578 | 1452 (-132) |
| H$_{methyl}$ symmetric stretch (W) | 2932 | 2927 | 2926 (-6) |
| H$_{methyl}$ asymmetric stretch (VW) | 2957 | 2954 | 2989 (35) |
| H$_{ring}$ symmetric stretch (M) | 3136 | 3135 | 3154 (18) |

[a] S, M, W, and VW indicate strong, medium, weak, and very weak peak intensities, respectively.

[b] The values in parentheses indicate differences between experimental and calculated results.
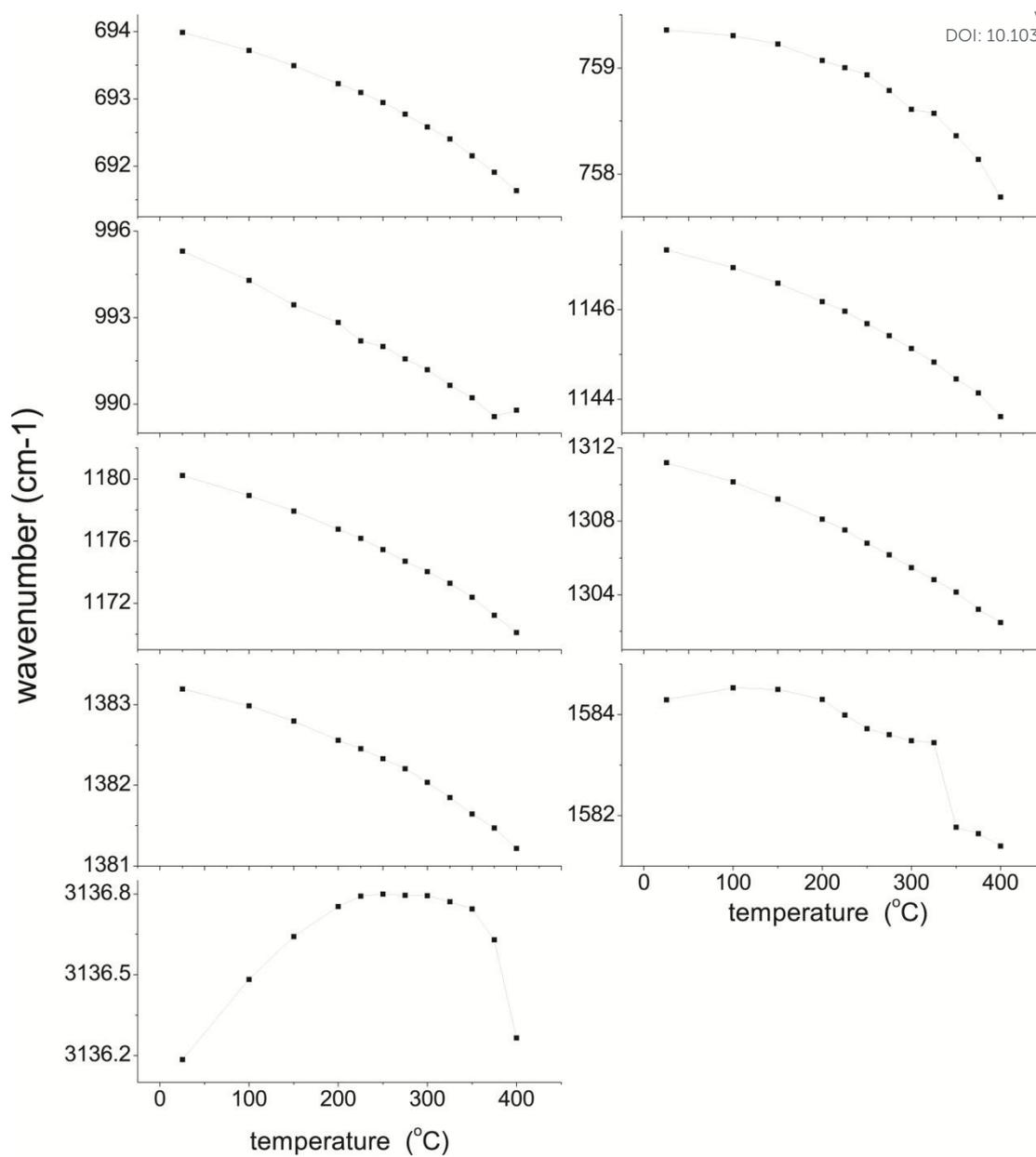
Figure S2 The peak position changes in temperature-dependent IR spectra of ZIF-8.
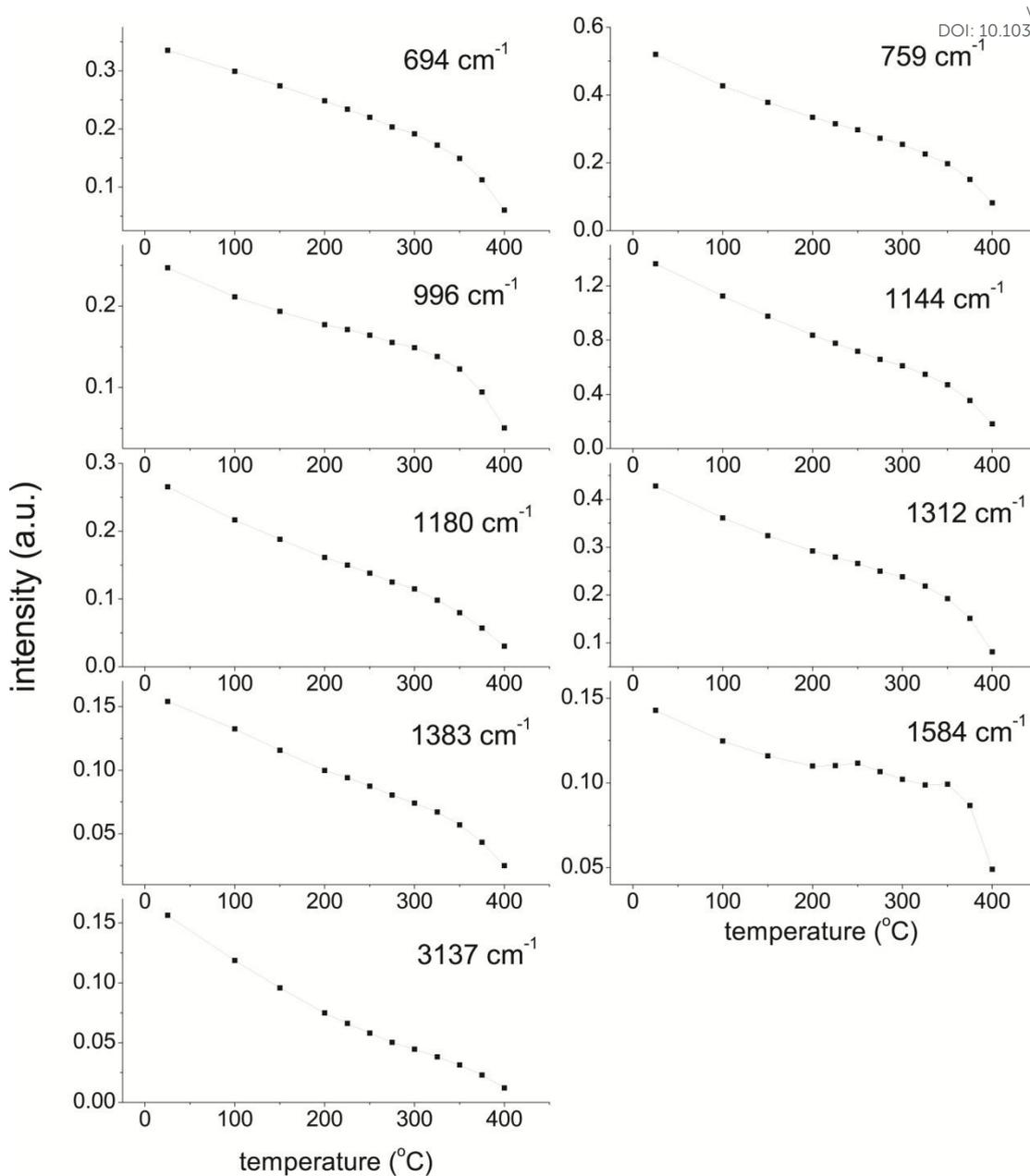
Figure S3 The peak intensity changes in temperature-dependent IR spectra of ZIF-8.
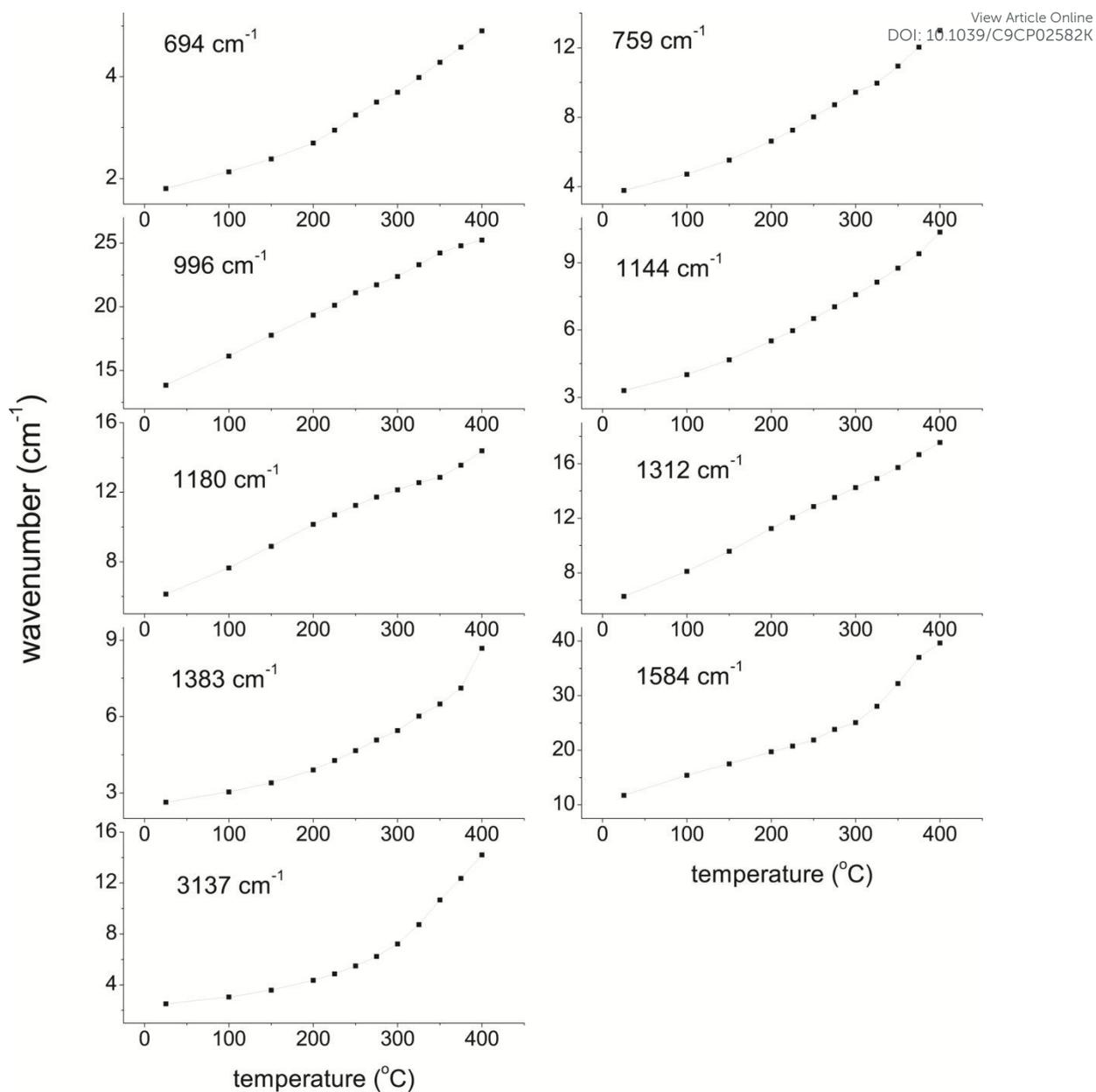
Figure S4 The peak width changes in temperature-dependent IR spectra of ZIF-8.
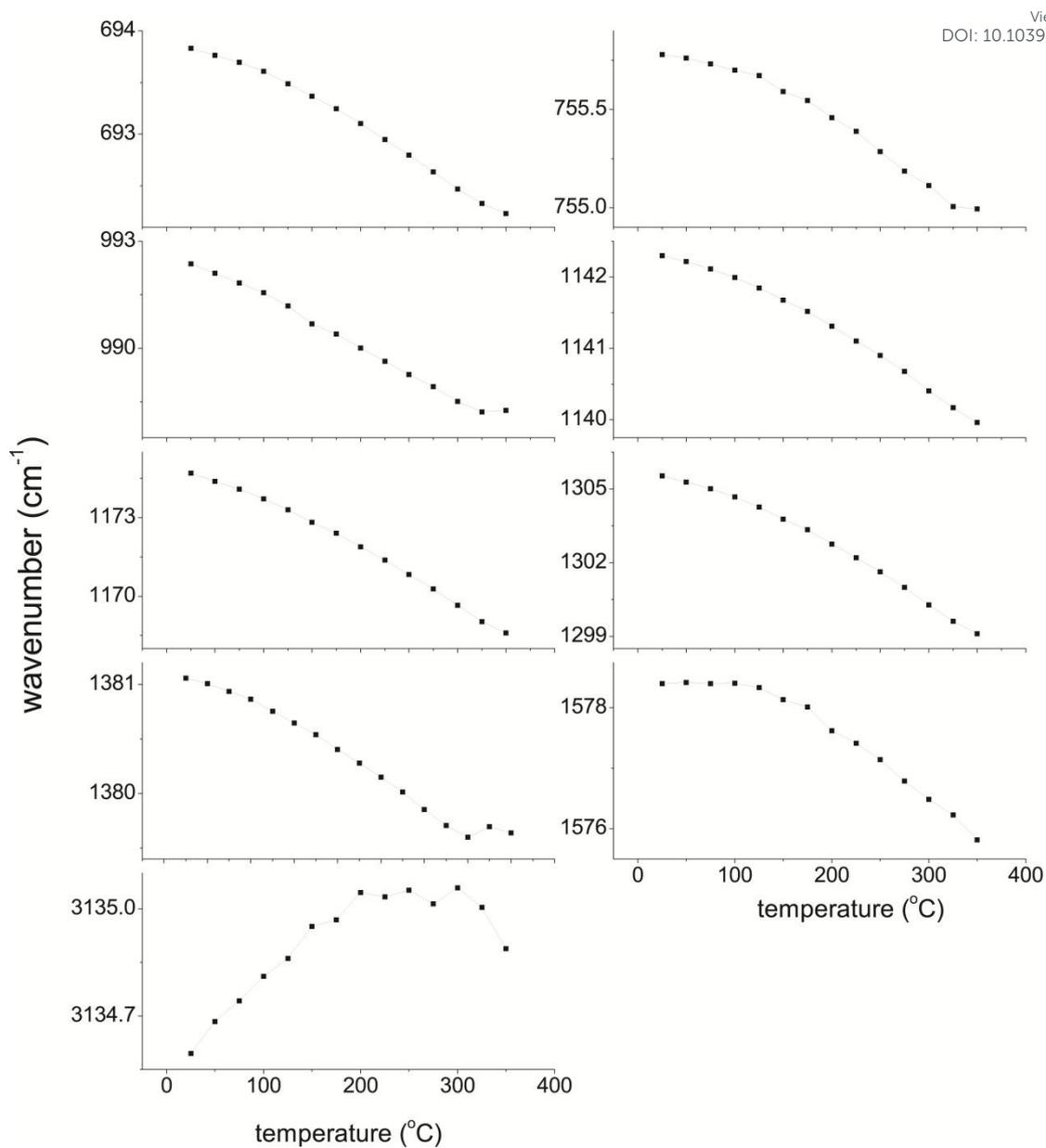
Figure S5 The peak position changes in temperature-dependent IR spectra of ZIF-67.
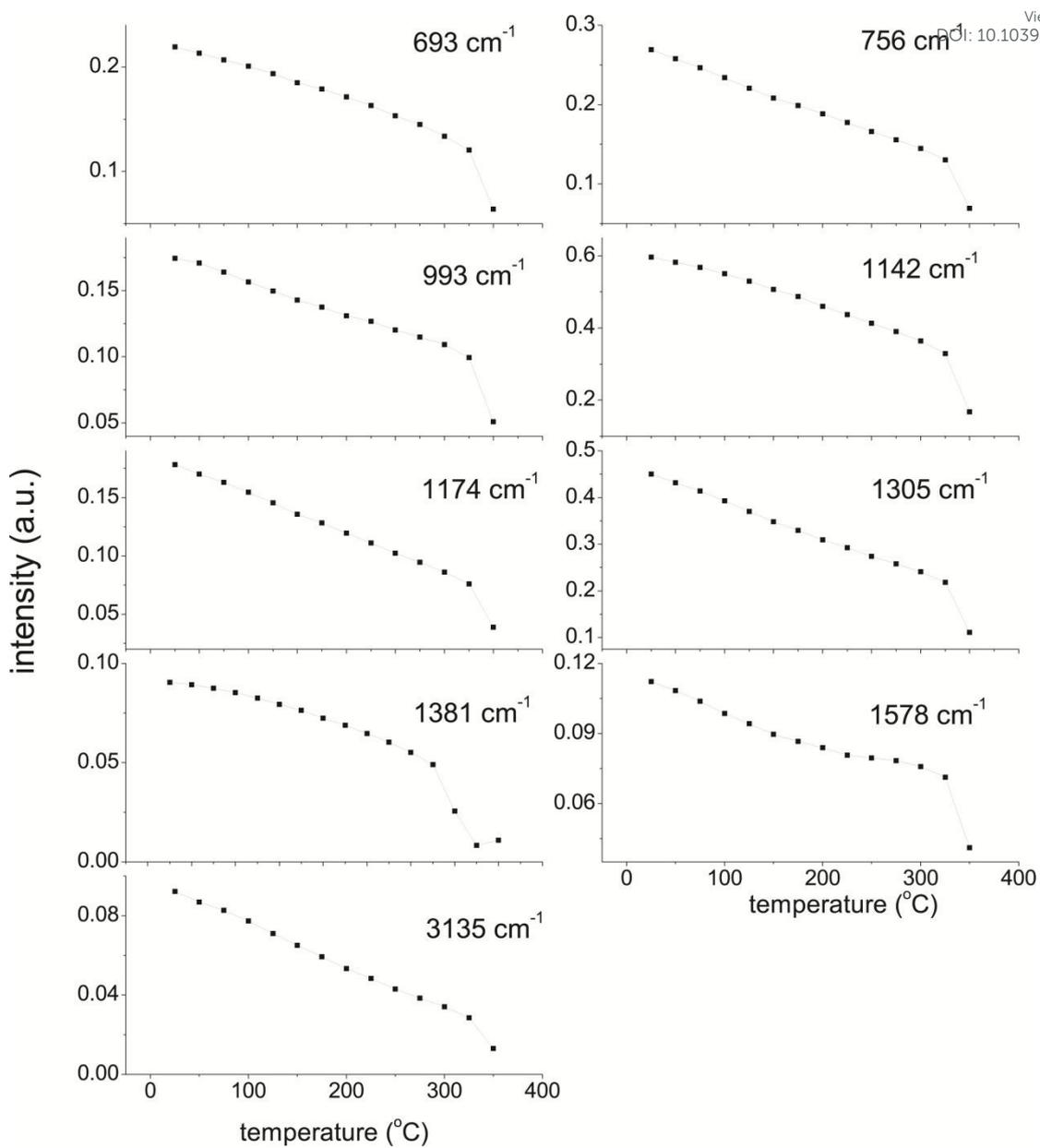
Figure S6 The peak intensity changes in temperature-dependent IR spectra of ZIF-67.
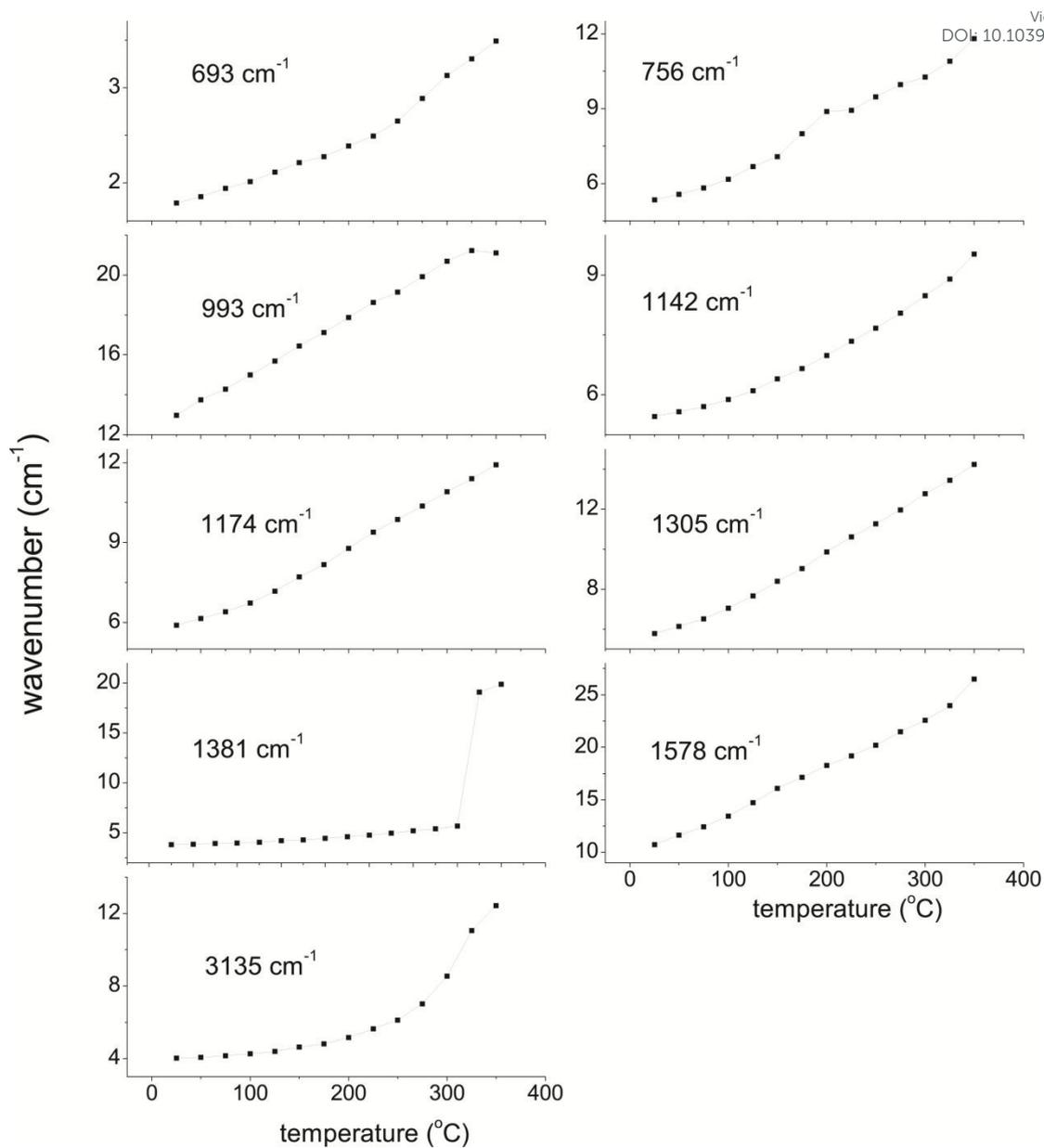
Figure S7 The peak width changes in temperature-dependent IR spectra of ZIF-67.

top view

side view

front view
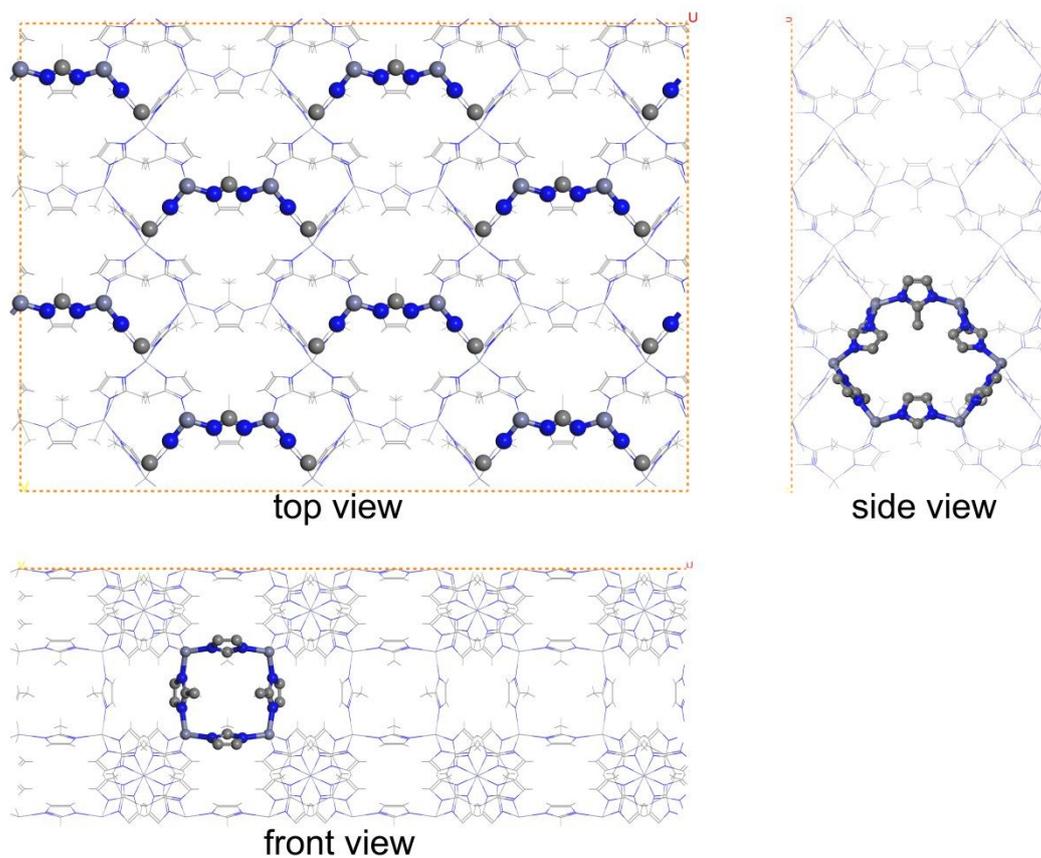
Fig. S8 The (011) plane of ZIF-8. The Co-N bonds are on this plane. The inter-planar distances are associated with the ZIF-8 frame. Hydrogen atoms are hidden for clarity.
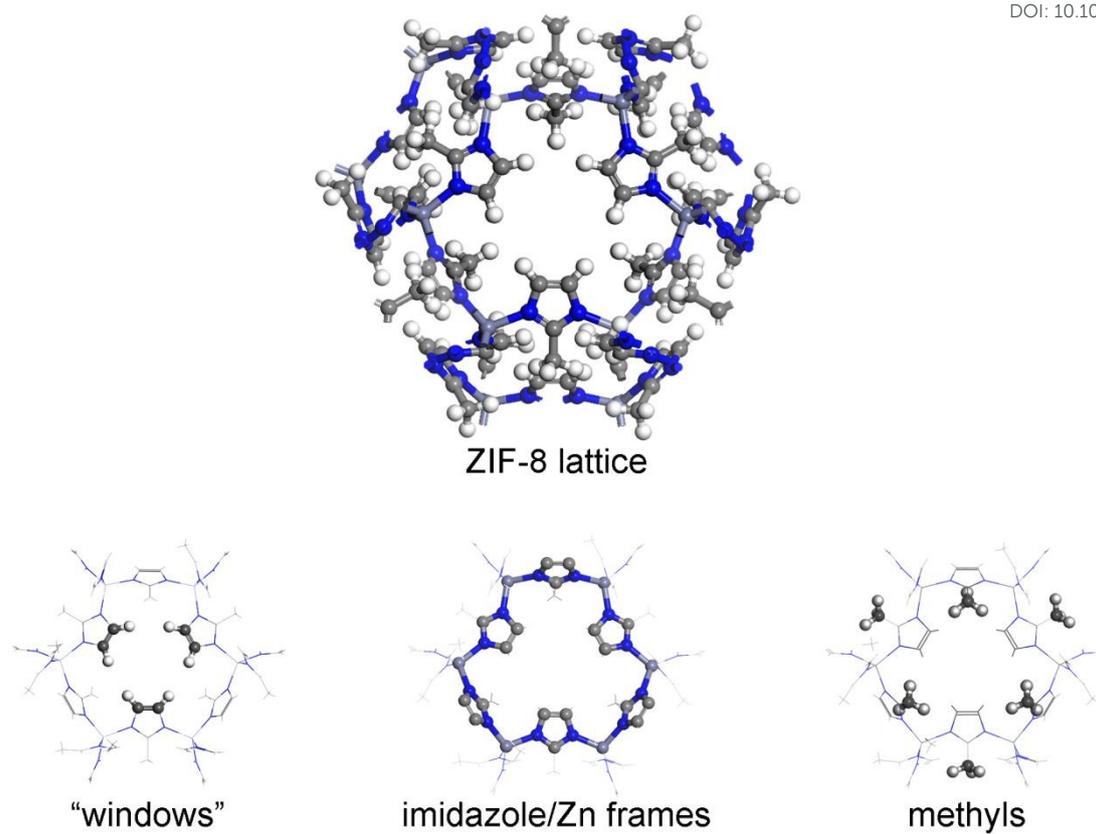
Figure S9 The lattice of ZIF-8/67. The lattice is composed of "window" fractions, "imidazole-metal" fractions, and "methyl" fractions. Zinc, nitrogen, carbon, and hydrogen atoms are purple, blue, grey, and white, respectively.
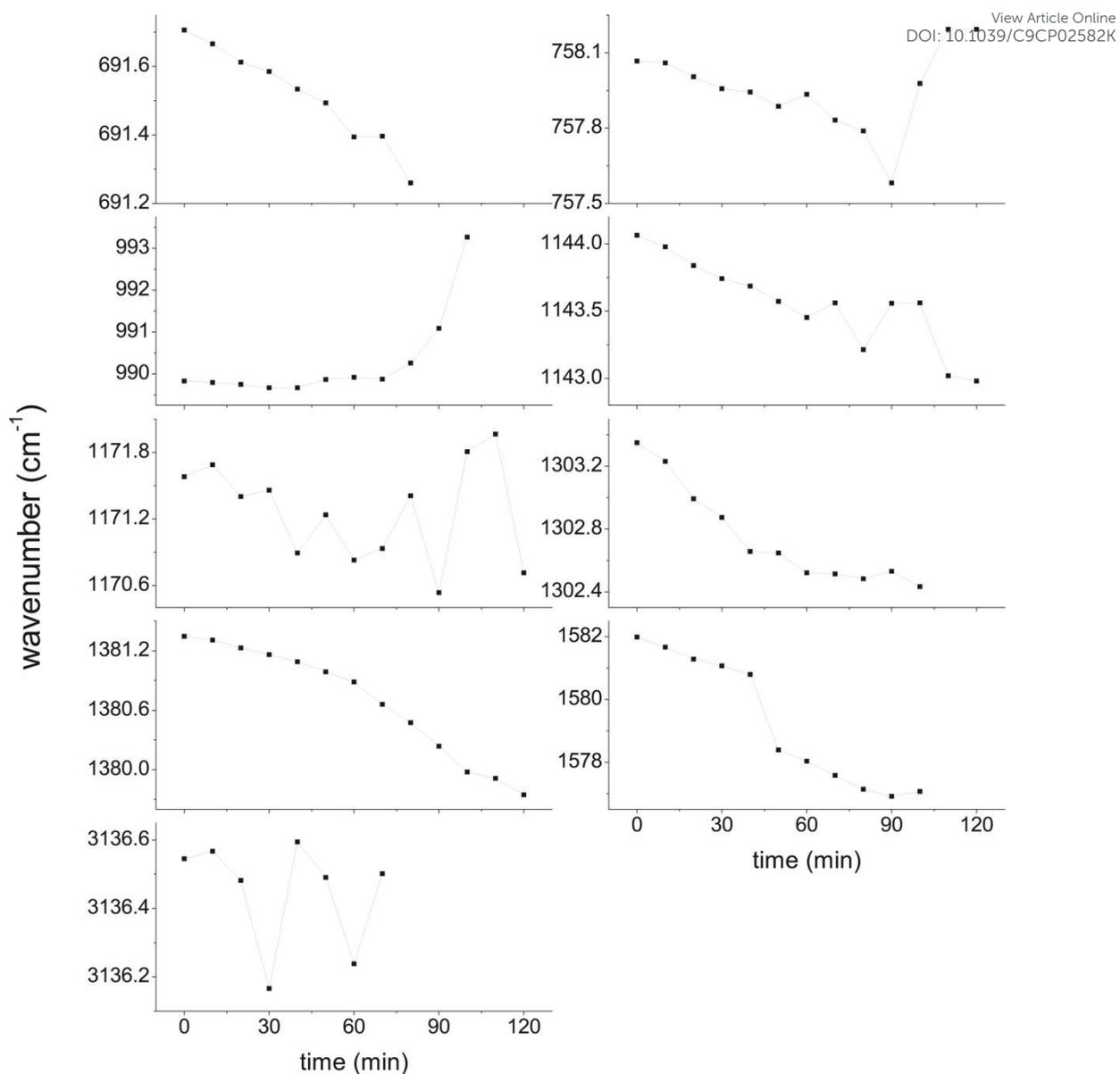
Figure S10 The peak position changes in time-dependent IR spectra of ZIF-8.
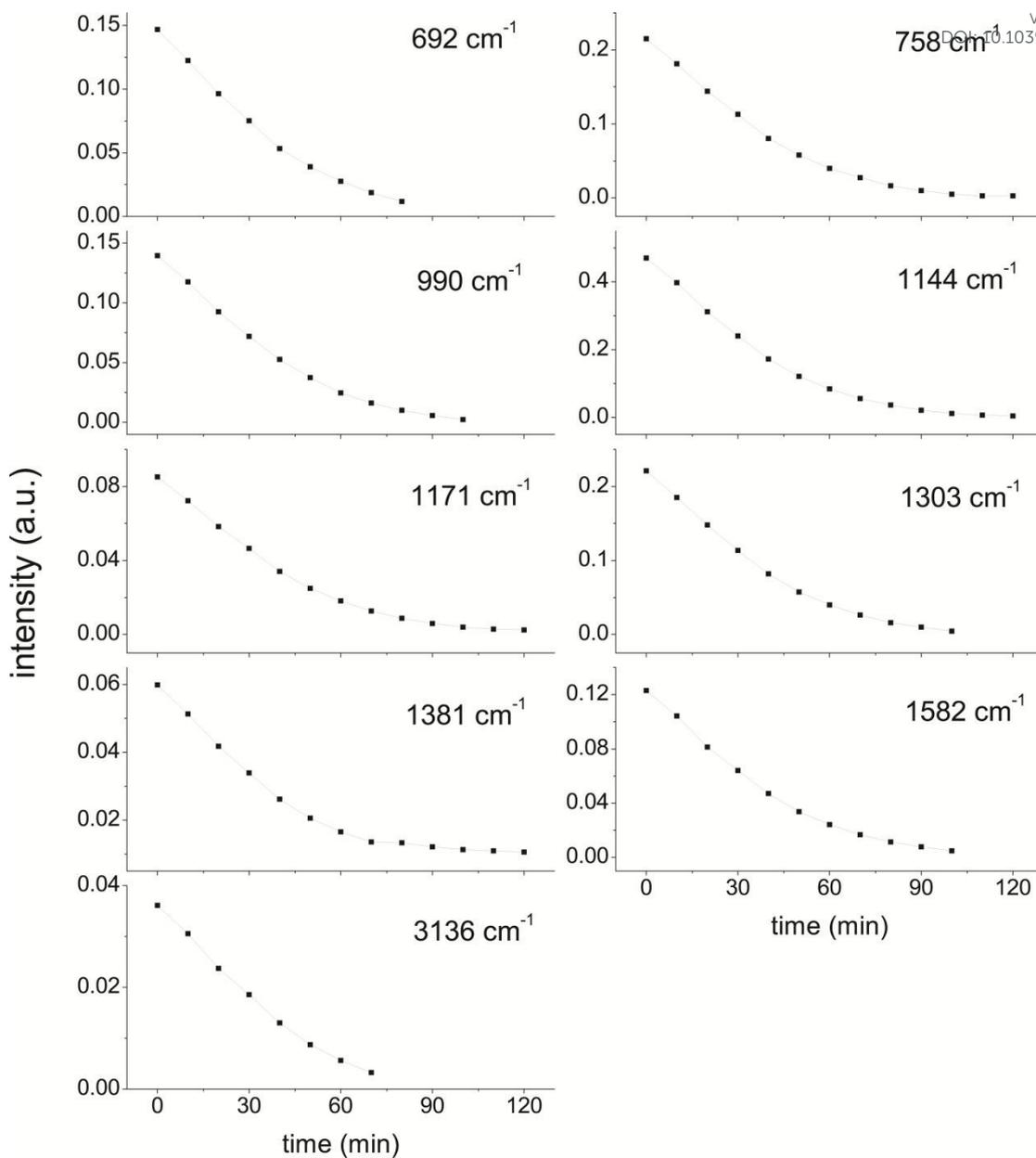
Figure S11 The peak intensity changes in time-dependent IR spectra of ZIF-8.
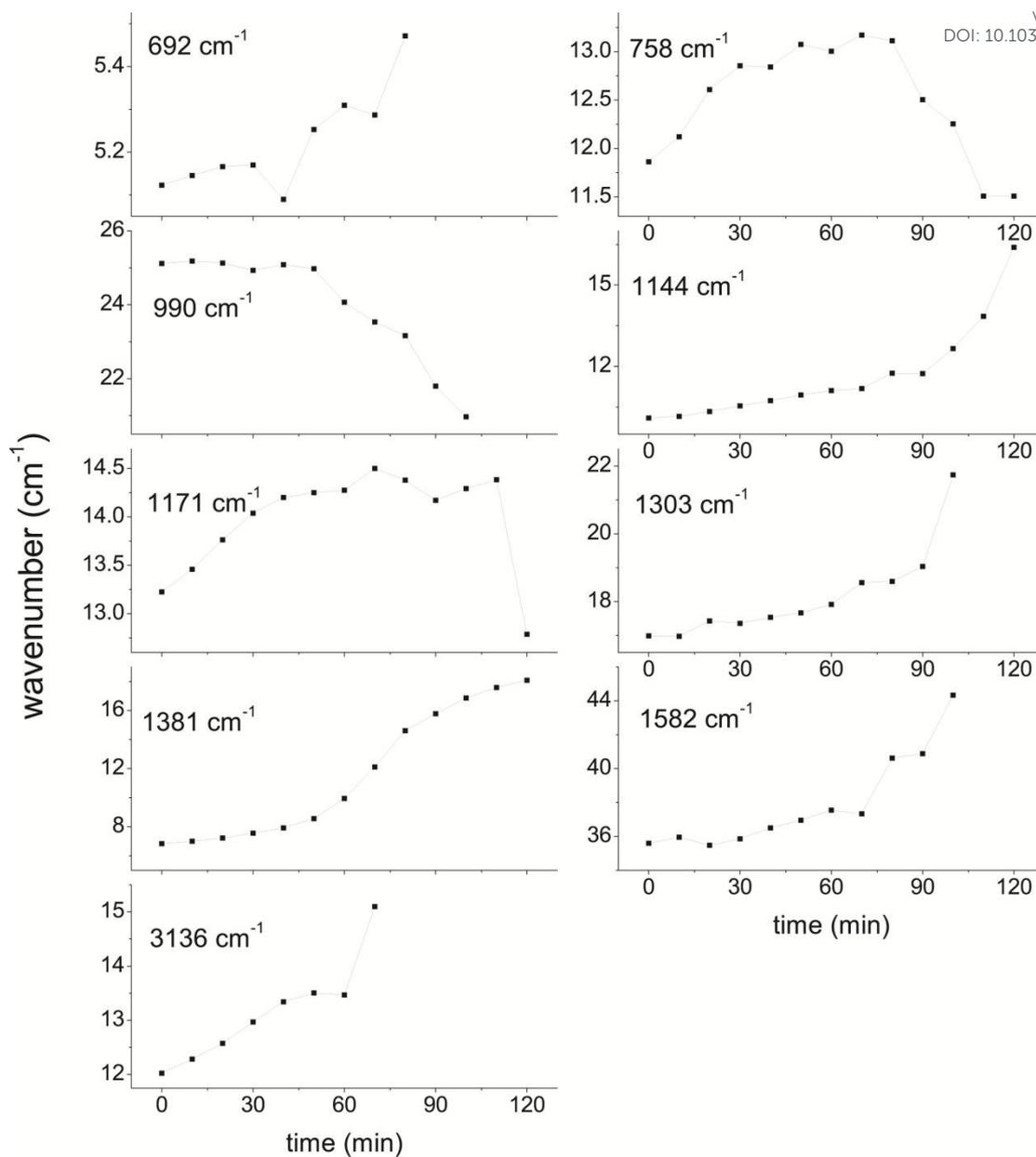
Figure S12 The peak width changes in time-dependent IR spectra of ZIF-8.
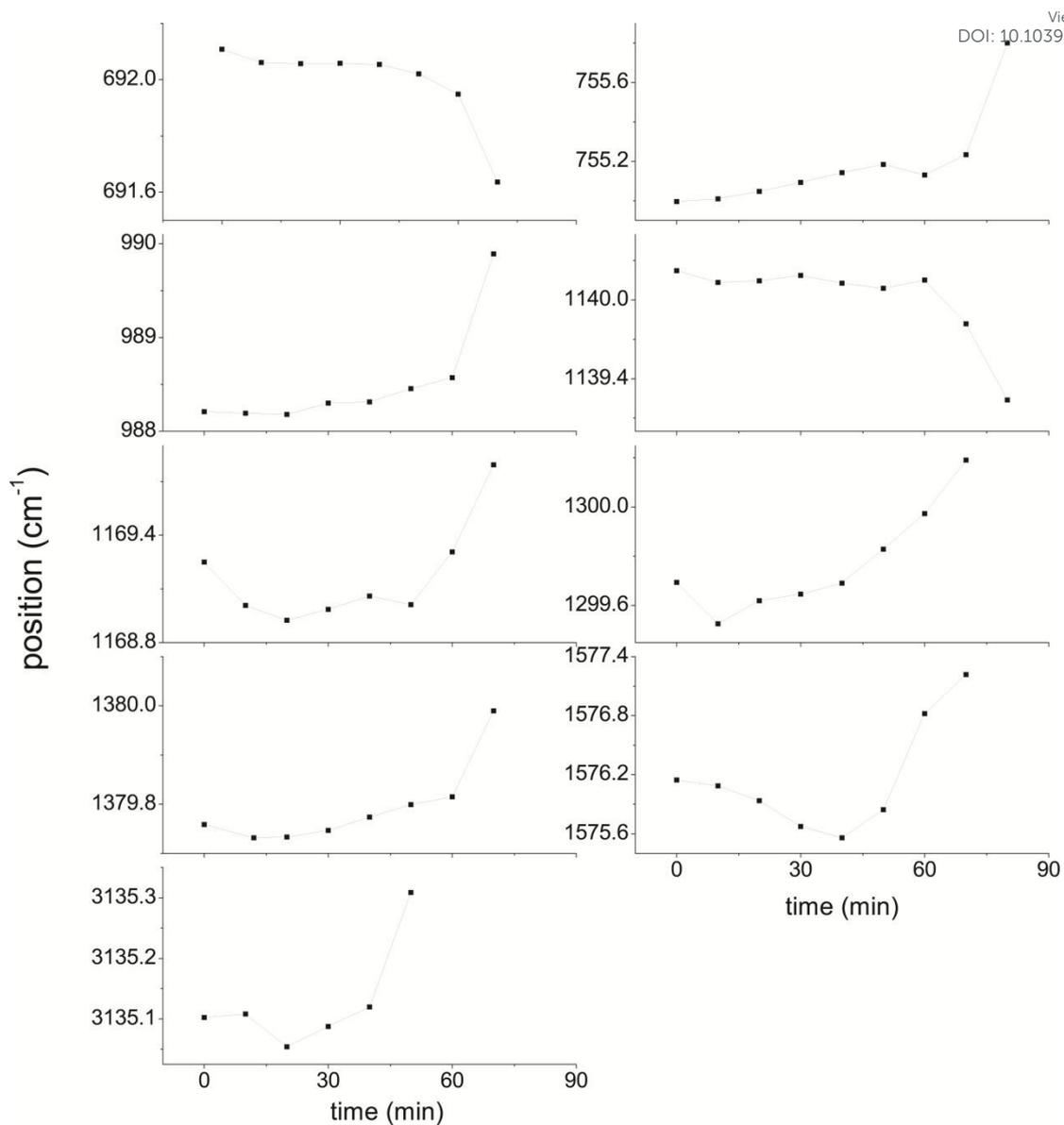
Figure S13 The peak position changes in time-dependent IR spectra of ZIF-67.
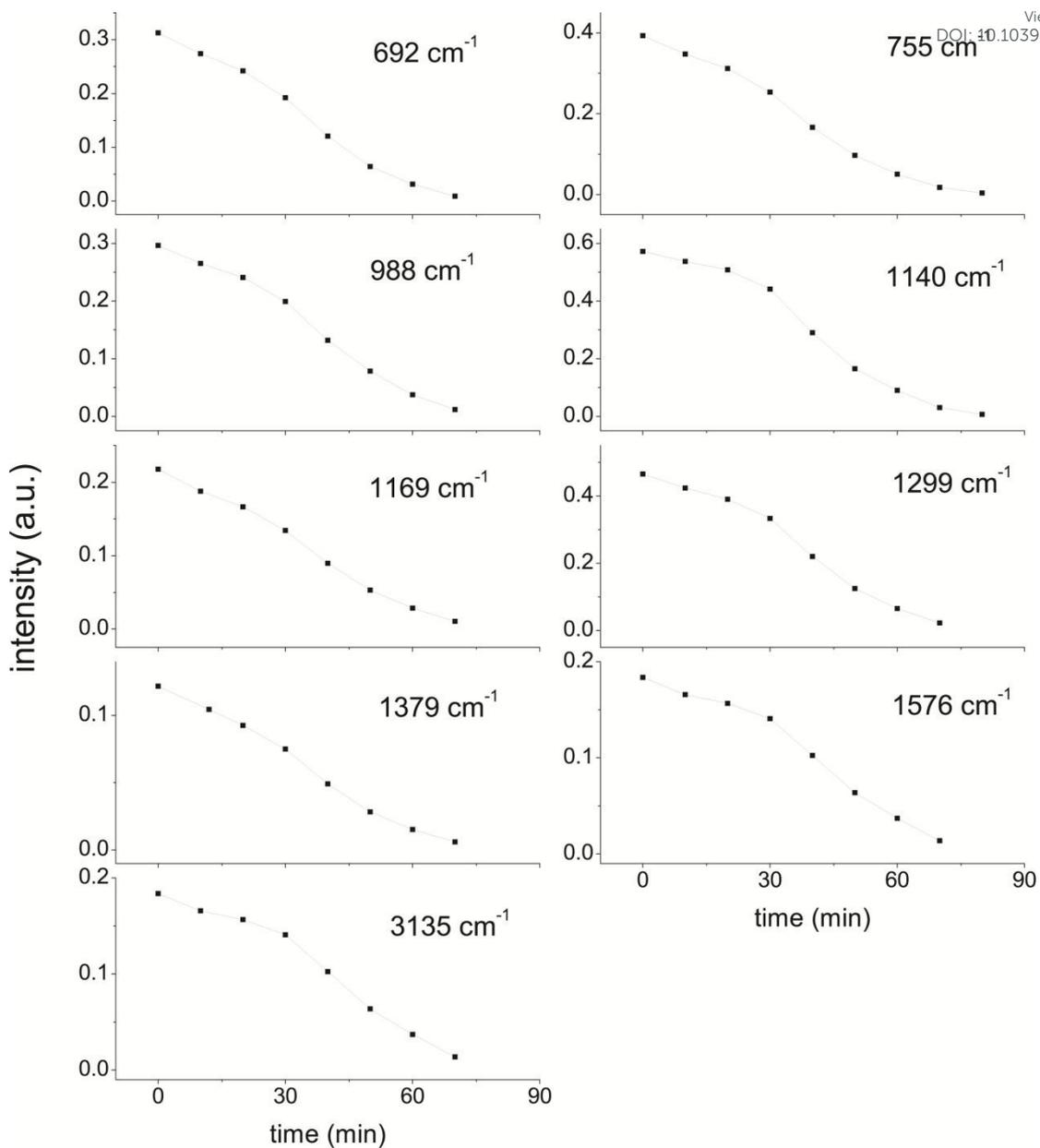
Figure S14 The peak intensity changes in time-dependent IR spectra of ZIF-67.
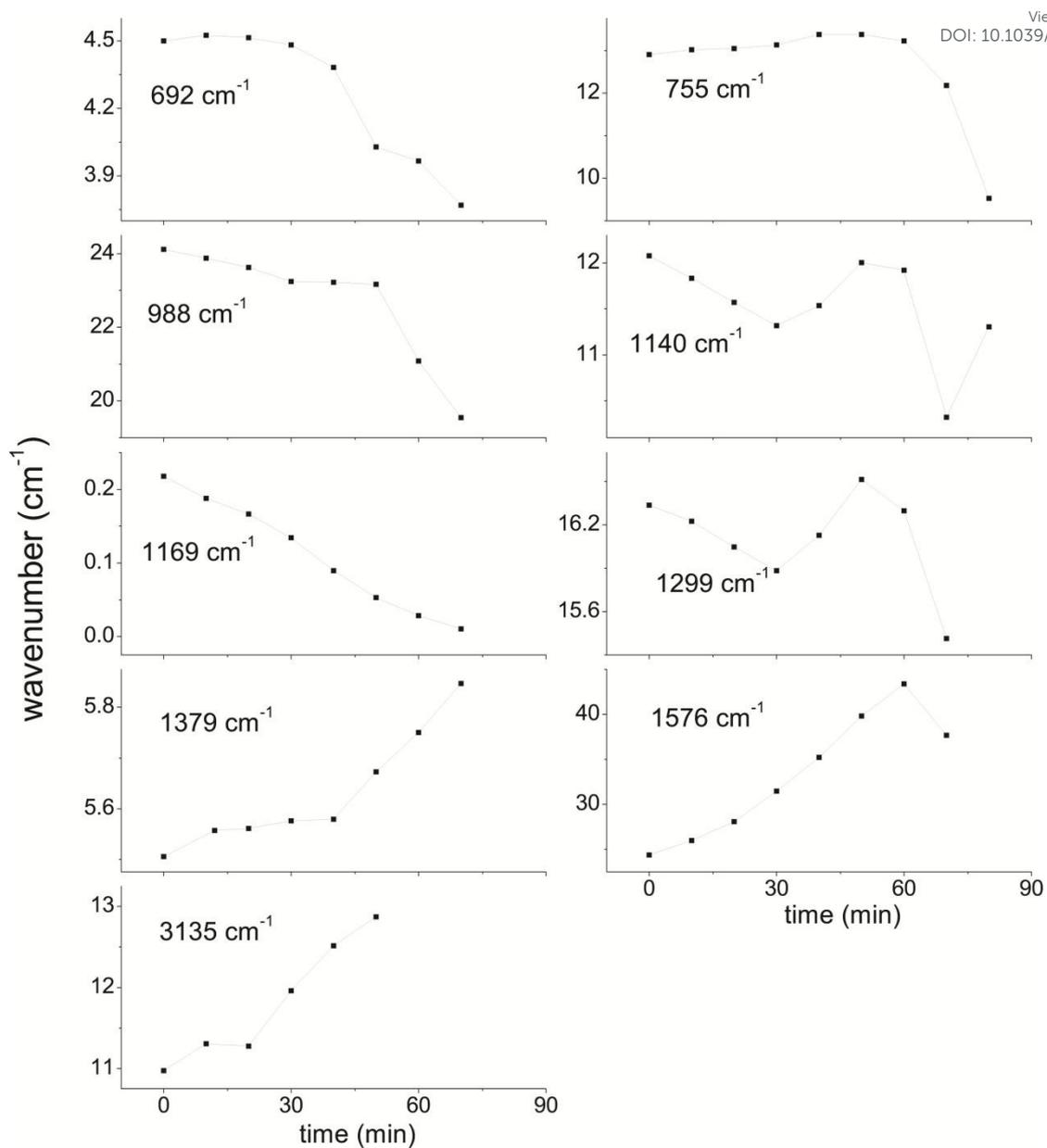
Figure S15 The peak width changes in time-dependent IR spectra of ZIF-67.

Table S2 The fitted results of $H_{ring}$ wagging intensity vs time plots to Avrami's model for both ZIF-8 and ZIF-67

|   | ZIF-8 | ZIF-67 |
| --- | --- | --- |
| $k$ | 0.0252±0.0001 | 0.0213±0.0003 |
| $n$ | 1.33±0.01 | 2.7±0.1 |
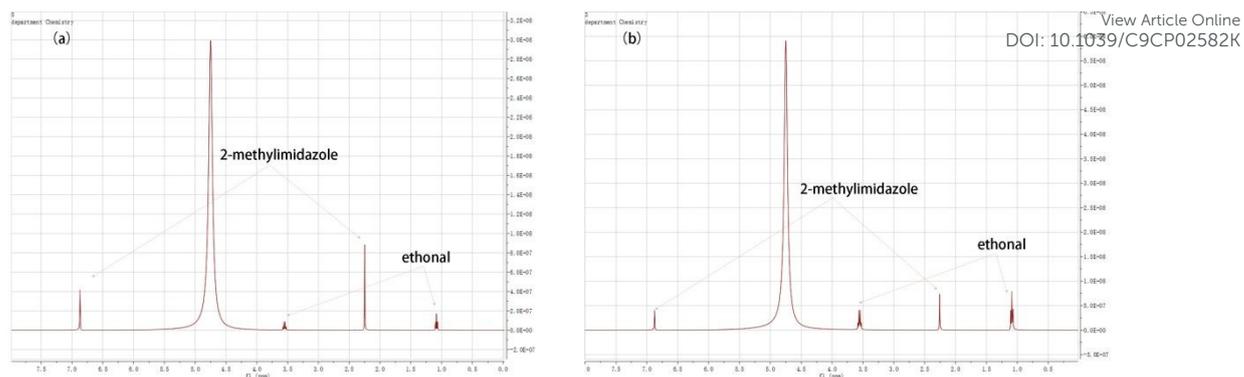
Figure S16 Solution NMR spectra of heated ZIF-8 (a) and ZIF-67 (b). ZIF-8 was heated at 350 ℃ for 20 minutes and ZIF-67 was heated at 300 ℃ for 10 minutes. The heated samples were immersed in $Na_2S$ deuterium oxide solution to obtain the solution for NMR measurements. It is clear that there are only 2-methylimidazole peaks and ethonal peaks (the samples were rinsed with ethonal). No other organic peaks were observed.